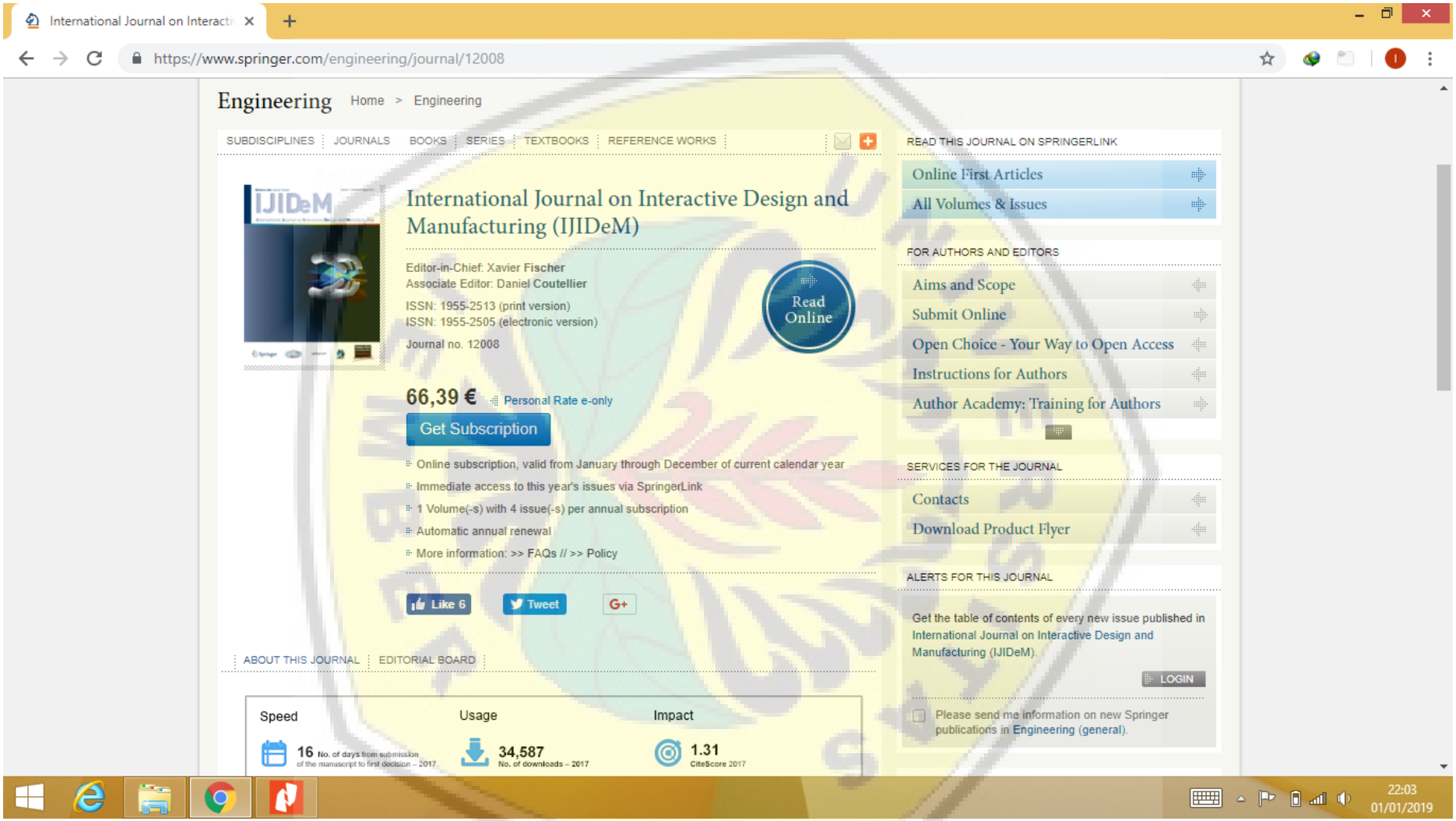

Volume 12, Issue 4, November 2018

ISSN: 1955-2513 (Print) 1955-2505 (Online)

In this issue (30 articles)

Page 2 of 2

International Journal on Interactive Design and Manufacturing (IJIDeM)
All Volumes & Issues
ISSN: 1955-2513 (Print) 1955-2505 (Online)

In this issue (30 articles)

Support

Damping properties and energy evaluation of a regenerative shock absorber

Ahmad Syuhri, Widyono Hadi & Skriptyan N. H. Syuhri

International Journal on Interactive Design and Manufacturing (IJIDeM)

ISSN 1955-2513
Volume 12
Number 4

Int J Interact Des Manuf (2018)
12:1385-1397
DOI 10.1007/s12008-017-0440-x

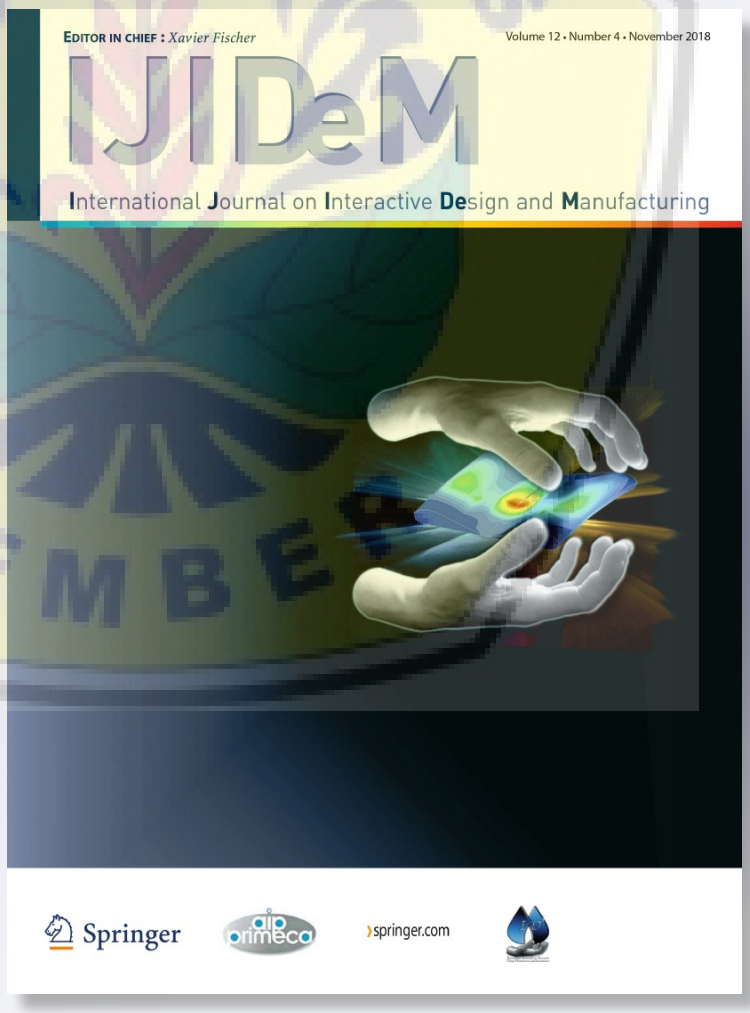

Springer

International Journal on Interactive Design and Manufacturing (IJIDeM) (2018) 12:1385–1397
https://doi.org/10.1007/s12008-017-0440-x

TECHNICAL PAPER

Damping properties and energy evaluation of a regenerative shock absorber

Ahmad Syuhri[1] · **Widyono Hadi**[2] · **Skriptyan N. H. Syuhri**[1]

Received: 5 August 2017 / Accepted: 29 November 2017 / Published online: 5 December 2017

Abstract

This paper presents dynamics analysis of a regenerative shock absorber using a linkage mechanism as motion transmission developed from a valid kinematics analysis. The main objective of this study is to obtain force and energy regeneration properties, which is followed by regeneration efficiency. Physical based models are adopted from the structural design and mathematical models are derived in order to conduct numerical investigations. Parameters are determined by estimation and measurement, while sinusoidal displacement input and its derivations are used to study system behaviors. In fixed amplitude and frequency, the total damping force is explored in time, displacement and velocity response, while regenerative power is compared to mechanical power in time domain for gaining efficiency. The result shows that asymmetry occurs in force–velocity curve which is influenced by mass inertias of epicyclic gears. In different amplitudes and frequencies, the damping nature, harvested power and efficiency are studied and linked with regard to the proportion of mechanical and electrical force. The result indicates that the electrical force has much contributed in low range of amplitudes and frequency, which is followed by energy harvesting and regeneration efficiency.

Keywords Dynamics analysis · Force characteristic · Energy regeneration · Arm mechanism · Regenerative shock absorber

List of symbols

F	Damping force
F_{AX}, F_{AY}, F_{AZ}	Force acting on point A parallel to the X-, Y-, Z, axes
F_{BX}, F_{BY}, F_{BZ}	Force acting on point B parallel to the X-, Y-, Z, axes
F_{CX}, F_{CY}, F_{CZ}	Force acting on point C parallel to the X-, Y-, Z, axes
F_{DX}, F_{DY}, F_{DZ}	Force acting on point D parallel to the X-, Y-, Z, axes
I	Electric current
J_{CD}	Moment of inertia of the rod CD
J_{c1}, J_{p1}, J_{s1}	Moment of inertia of the carrier, the planet gear and the sun gear in the first stage of epicyclic gears
J_{c2}, J_{p2}, J_{s2}	Moment of inertia of the carrier, the planet gear and the sun gear in the second stage of epicyclic gears
J_{eq}	Equivalent moment of inertia of the epicyclic gears
J_G	Moment of inertia of the generator rotor
L_{ADX}, L_{ADY}, L_{ADZ}	Length of the rod AD with respect to X-, Y-, Z-components
L_{BCX}, L_{BCY}, L_{BCZ}	Length of the rod BC with respect to X-, Y-, Z-components
L_{CDX}, L_{CDZ}	Length of the rod CD with respect to X- and Z-components
$\overline{M}_A$, $\overline{M}_B$	Sum of moments of all external forces acting about a fixed point A and B
m_{p1}, m_{p2}	Mass of the planet gear in the first stage and the second stage of epicyclic gears

✉ Ahmad Syuhri
ahmad.syuhri@unej.ac.id

Widyono Hadi
widyono@unej.ac.id

Skriptyan N. H. Syuhri
skriptyan.syuhri@unej.ac.id

[1] Department of Mechanical Engineering, University of Jember, Jember 68121, Indonesia

[2] Department of Electrical Engineering, University of Jember, Jember 68121, Indonesia

n_1, n_2	Total number of planet gears in the first stage and the second stage of epicyclic gears
n_{p1}, n_{r1}, n_{s1}	Number of teeth of each planet gear, the ring gear and the sun gear in the first stage of epicyclic gears
n_{p2}, n_{r2}, n_{s2}	Number of teeth of each planet gear, the ring gear and the sun gear in the second stage of epicyclic gears
r_{c1}, r_{c2}	Radius of the carrier in the first stage and the second stage of epicyclic gears
T_G, T_e, T_{PG}	Torque of the generator, electric load and epicyclic gears
V	Electric voltage
α_O	Angular acceleration with respect to point O
α_{c1}	Angular velocity of the carrier in the first stage of epicyclic gears
α_G	Angular acceleration of the generator rotor
$\hat{i}, \hat{j}, \hat{k}$	Directions of the moving axes and fixed to the X-, Y-, Z-axes
θ_O	Rotation of the bottom plate with respect to point O
$\omega_{c1}, \omega_{p1}, \omega_{s1}$	Angular velocity of the carrier, the planet gear and the sun gear in the first stage of epicyclic gears
$\omega_{c2}, \omega_{p2}, \omega_{s2}$	Angular velocity of the carrier, the planet gear and the sun gear in the second stage of epicyclic gears
ω_G	Angular velocity of the generator rotor
ω_O	Angular velocity of the bottom plate with respect to point O

1 Introduction

The regenerative shock absorbers have recently attracted great attention by many researchers since compromising with a green energy in the case of automotive application. Beside harvesting as much as energy from dissipated energy, the RSA needs to maintain flexibility, to improve performances and to utilize harvested energy in vehicle [1]. The RSA itself generally consists of a transmission that transmit reciprocating motion into desired motion, and an electrical converter that turns mechanical energy into electrical energy. Transmissions such as hydraulic motor, rack-pinion system, ball screw mechanism and linkage mechanisms can be used for converting linear motion into rotary motion, which is suitable input for rotary generator [2]. Other transmission that alters vertical input into axial output as developed by Hendrowati et al. [3] can be used for inducing a multi layer piezoelectric. However, the transmission may not be required in an electrical converter such as a linear generator which generating electrical energy when a relative position between the magnet array and the coils linearly cuts the magnetic line [4].

Force characteristic performed by the RSA is such a unique and different compared with a traditional shock absorber (TSA). In TSA, the damping force, which is mainly influenced by hydraulic orifice compensation, has actually asymmetric and slightly hysteretic characteristic [5]. Asymmetry in rebound and compression of force characteristic plays important role in terms of vehicle stability and ride comfort [6,7]. In the case of RSA, for instance, rack-pinion-RSA has symmetric, hysteretic and negative slope characteristic in force–displacement loops that proportionally comes from mass inertias and electric load [8,9]. Ball screw-RSA exhibits similar properties with the rack-pinion-RSA where it is identically formed by a negative stiffness and a damping derived from acceleration and velocity functions, respectively [4,10]. The following characteristics are also occurred in linkage-RSA where a complex algebraic mechanism with less mass inertia and friction is used to convert linear motion into rotary motion [11,12]. Linear electromagnetic-RSA has faintly hysteresis and highly symmetry derived from a velocity function of a linear generator [13,14]. However, hydraulic-RSA has naturally close performance to TSA, where it is simply modified from a hydraulic cylinder and combined with additional energy harvesting equipments [15–19].

Based on the importance of asymmetry, some methods have been suggested either electrically or mechanically for improving characteristics of the RSA. Li et al. [8] proposed a control circuit by means of splitting positive and negative voltage direction with different load, which leads to asymmetric characteristic in force–velocity loops. In the case of the RSA using mechanical motion rectifier as developed in [9,20,21], different gear ratio will mechanically lead to distinct the rectification result that produce asymmetry behavior [22]. Unfortunately, these all methods will produce different energy harvested in rebound and compression stage. The need of symmetrical properties in the energy regeneration is necessary that will directly influence for the total efficiency.

An arm mechanism, proposed by Maravandi [2], is one kind of linkage mechanisms utilized as motion converter that authentically has different characteristics in rebound and compression [23,24]. From kinematics analysis studied in [25], this mechanism has nearly ellipse with different eccentricity in the displacement–angular velocity relationship, while different peaks in positive and negative sign of angular acceleration are obtained in the displacement–angular acceleration loops. This exemplifies an advantage in

the RSA to carry out asymmetry in term of force characteristics and symmetry in term of energy regeneration.

Based on the previous kinematics derivation, this paper aims to conduct dynamics analysis of force characteristics and energy regeneration in the RSA using the arm mechanism. The main contributions are (1) to study the dynamics behavior of the RSA regarding kinematics analysis; (2) to investigate the influences of mechanical and electrical parameters for total damping force and energy regeneration; and (3) to create the physical based model, which can be functioned to rapid development in the future. The dynamics behavior and its influences in this study will enhance the behavioral component model, which is part of modeling for interactive design and manufacturing. The interactive aspect from this design can be interpreted by illustrating the meaningful component properties in interactive ways such as figuring the time responses, dynamics responses including displacement and velocity, and 3D surfaces. This allows readers in order to bridging the designs and requirements in an engineering system before it leads to manufacturing and testing section.

In order to achieve the objective, design of the RSA including structural design and dynamics modeling of the mechanical system is derived in Sects. 2.1–2.3. Parameter identification from experimental data for an energy regeneration unit is presented in Sect. 2.4. The total damping force equation is then revealed in Sect. 2.5. Input and parameter for numerical simulation are obtained based on calculation and direct measurement in Sect. 3. Simulation analysis involving force and energy regeneration in terms of time, displacement, velocity is performed in Sect. 4.1, while the comparisons are executed for different amplitudes and frequencies in Sect. 4.2. Finally, conclusions are drawn in Sect. 5.

2 Design and modeling

2.1 Design layout

The proposed design of the RSA and energy regeneration unit is depicted in Fig. 1. Overall, the RSA comprises of an arm mechanism, a bearing, epicyclic gears and a direct current (DC) generator while the energy regeneration unit is arranged by a DC booster and a 12 V battery. The arm mechanism is mainly composed by an upper plate, a bottom plate, two rods and ball joints in which it is attached in each ends of the upper plate and the bottom plate for connecting the rods. In order to work as a linear-to-rotary motion device, the upper plate can only work in a translation motion whereas the bottom plate can only perform in a rotation motion. Consequently, the rods with certain initial angle can rotate the bottom plate when a sufficient force is applied on the upper plate via the top mount. The epicyclic gears system, which is coupled by the bottom plate, significantly increases the

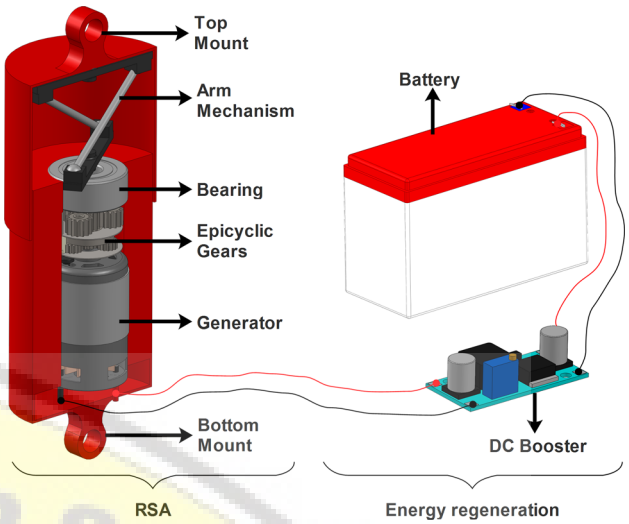

Fig. 1 Structure layout of RSA and energy regeneration unit

driving speed of the generator. Electricity produced by the generator is therefore processed by the DC booster. Here the DC booster is functioned not only to enhance the voltage until exceeded 12 V but also to keep the voltage under 15 V. This configuration is to prevent any damage in the battery when a charging process occurs. Furthermore, the charging process is determined as load of the generator while this load will totally influence for the RSA behavior.

2.2 Arm mechanism

This section derives only the dynamic analysis of the arm mechanism whereas the kinematic analysis was done and validated in [25] and described in "Appendix". Hence, the configurative model of the arm mechanism including notations and free body diagrams is illustrated in Fig. 2. When a force is applied in the middle of the upper plate in Y-axis, the reaction forces both in A point and B point will be half of the force applied due to symmetrical structure. These forces are then distributed in the rod AD and BC so the rods will definitely work on three axes. By applying the equations of equilibrium and the resultant moment produced by 3D force about a turning point of A and B, the following equations can be obtained as follows,

$$\begin{cases} F_{AX} = F_{DX} \\ F_{AY} = F_{DY} \\ F_{AZ} = F_{DZ} \\ \overline{M}_A = -\left(L_{ADY}F_{DZ} + L_{ADZ}F_{DY}\right)\hat{i} + \left(L_{ADX}F_{DZ} - L_{ADZ}F_{DX}\right)\hat{j} \\ \qquad -\left(L_{ADX}F_{DY} + L_{ADY}F_{DX}\right)\hat{k} \end{cases} \tag{1}$$

$$\begin{cases} F_{BX} = F_{CX} \\ F_{BY} = F_{CY} \\ F_{BZ} = F_{CZ} \\ \overline{M}_B = \left(L_{BCY}F_{CZ} + L_{BCZ}F_{CY}\right)\hat{i} + \left(L_{BCX}F_{CZ} - L_{BCZ}F_{CX}\right)\hat{j} \\ \qquad +\left(L_{BCX}F_{CY} + L_{BCY}F_{CX}\right)\hat{k} \end{cases} \tag{2}$$

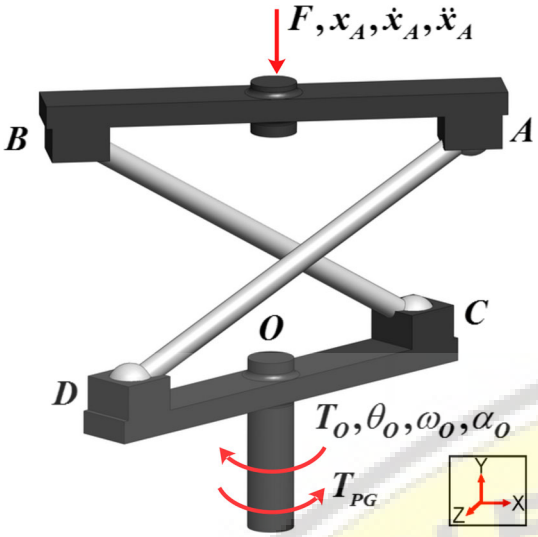

Fig. 2 Free body diagram of the arm mechanism and its moving directions

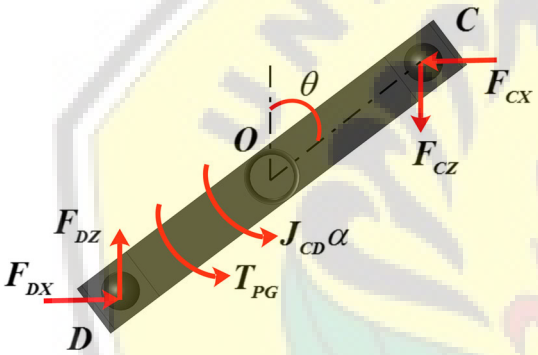

Fig. 3 Free body diagram of the bottom plate in XZ-plane

Forces and torques worked in the bottom are drawn in Fig. 3 with respect to the XZ-plane. Here the bottom plate is designed with particular mass so the moment of inertia in this part is taken into account. The moment equations can now be equated with respect to the turning point (O) of the bottom plate, which yields,

$$0.5L_{CDX}\left(F_{CZ}+F_{DZ}\right)-0.5L_{CDZ}\left(F_{CX}+F_{DX}\right) = J_{CD}\alpha_o + T_{PG} \tag{3}$$

where $0.5L_{CDX} = 0.5L_{CD}\sin\theta_O$ and $0.5L_{CDZ} = 0.5L_{CD}\cos\theta_O$.

The relation between force and torque in the upper plate and the bottom plate, respectively, can be given by equating $\hat{i}$, $\hat{j}$, $\hat{k}$ component from Eqs. (1) and (2) then substituting those results into Eq. (3) as follows,

$$0.5L_{CDZ}\left(\frac{L_{BCZ}}{L_{BCY}}F_{CY}+\frac{L_{ADZ}}{L_{ADY}}F_{DY}\right) - 0.5L_{CDX}\left(\frac{L_{BCX}}{L_{BCY}}F_{CY}+\frac{L_{ADX}}{L_{ADY}}F_{DY}\right) = J_{CD}\alpha_o + T_{PG} \tag{4}$$

where F_{CY} and F_{DY} signify F_{BY} and F_{AY}, respectively. In the upper plate body, F_{AY} and F_{BY} are equal with $0.5F$. On the other hand, the symmetrical system will produce equal length of the rods that means $L_{AD(X,Y,Z)} = L_{BC(X,Y,Z)}$. Hence, Eq. (4), computed with respect to F, can be reformed as follows,

$$F = \frac{J_{CD}\alpha_o + T_{PG}}{L_{CDZ}\left(\frac{L_{ADZ}}{L_{ADY}}\right) - L_{CDX}\left(\frac{L_{ADX}}{L_{ADY}}\right)} \tag{5}$$

2.3 Epicyclic gears

The overall structure of the epicyclic gears is shown in Fig. 4a where the detailed parts of the gears are illustrated in Fig. 4b. The subscripts 1 and 2 indicate first and second stage of the epicyclic gear, respectively. Here we use the two stage planetary gear to increase the velocity transmitted into the generator in which frictional loss in each stage is assumed of 20%. In this configuration, the $Carrier_1$ and the $Sun\ Gear_2$ designate as the input and the final output of rotation, respectively. The ring gear both in first stage and in second stage is fixed from rotation. It is obtained in Fig. 4b that the $Sun\ Gear_1$ is directly coupled with the $Carrier_2$. Consequently, ω_{s1} satisfies ω_{c2}. The velocity in each gear can then be obtained with respect to the $Carrier_1$ as follows,

$$\begin{cases} \omega_{p1} = \left(1-\frac{n_{r1}}{n_{p1}}\right)\omega_{c1} \\ \omega_{s1} = \left(1+\frac{n_{r1}}{n_{s1}}\right)\omega_{c1} \\ \omega_{p2} = \left(1-\frac{n_{r2}}{n_{p2}}\right)\left(1+\frac{n_{r1}}{r_{s1}}\right)\omega_{c1} \\ \omega_{s2} = \left(1+\frac{n_{r2}}{n_{s2}}\right)\left(1+\frac{n_{r1}}{n_{s1}}\right)\omega_{c1} \end{cases} \tag{6}$$

By using the velocity relationships in each gear, the equivalent moment of inertia can be obtained using the kinetic energy made by systems. Hence, the equivalent moment of inertia of the epicyclic gear, regarded with reference to the $Carrier_1$, can be given as follows,

$$J_{eq} = J_{s1}\left(\frac{\omega_{s1}}{\omega_{c1}}\right)^2 + \left(J_{c1}+n_1 m_{p1} r_{c1}^2\right) + n_1 J_{p1}\left(\frac{\omega_{p1}}{\omega_{c1}}\right)^2 + J_{s2}\left(\frac{\omega_{s2}}{\omega_{c1}}\right)^2 + \left(J_{c2}+n_2 m_{p2} r_{c2}^2\right)\left(\frac{\omega_{c2}}{\omega_{c1}}\right)^2 + n_2 J_{p2}\left(\frac{\omega_{p2}}{\omega_{c1}}\right)^2 \tag{7}$$

The free body diagram of the planetary gears can now be simply modeled as a rigid body with reference to the velocity of the $Carrier_1$. By applying d'Alembert law's, the following equation can be therefore derived as follows,

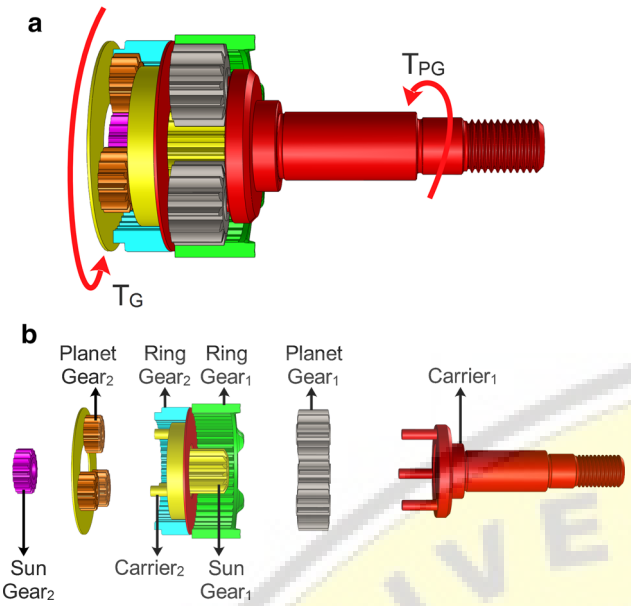

Fig. 4 **a** Overall structure of the planetary gears; **b** the exploded view of the planetary gears

$$J_{eq}\alpha_{c1} + T_G\left(\frac{\omega_{s2}}{\omega_{c1}}\right) = T_{PG} \tag{8}$$

where T_G is defined by addition of mechanical torque and electrical torque of the generator as follows,

$$J_G\alpha_G + T_e = T_G \tag{9}$$

2.4 Energy regeneration

2.4.1 Experimental data

To acquire electrical parameters, the energy regeneration unit is tested under typical and constant velocity. The results are then obtained as current and voltage generated with respect to angular velocity (rad/s). The experiment results are plotted in Fig. 5. The current generated from experimental data with respect to angular velocity, marked as circle, is plotted in Fig. 5a. By simply applying linear regression, the least-squares fit is achieved as follows,

$$I\left(\omega_G\right) = 0.001008\omega_G - 0.02753 \tag{10}$$

where this equation is only valid for $\omega_G \geq 27.31$ rad/s. The comparison between least-square approximation and experimental data is shown in Fig. 5a. This approximation produces R-square about 0.9902 so that means 99.02% of the experimental data has been represented by the linear model.

Figure 5b shows the experimental voltage data, which has a nonlinear relationship with respect to angular velocity. To signify a best-fit approximation, we split the data based on angular velocity into two regions. The first region is when the voltage increases very rapidly. The second region is when it increases gradually. These two regions fulfill the exponential model and the linear model.

By applying nonlinear regression and linear regression, respectively, the following equations associated with these can therefore be obtained as follows,

$$V\left(\omega_G\right) = \begin{cases} \left(7.248 \times 10^{-9}\right) e^{0.461\omega_G}, & \omega_G \leq 46.2 \\ 0.0007748\omega_G + 12.93, & \omega_G > 46.2 \end{cases} \tag{11}$$

where these approximations have R-square about 93.46 and 68.66%, respectively. Considering the Kirchhoff's voltage law, the voltage has a linear model that means the first region, represented with exponential model in Eq. (11), must be linearized to merit with the equation.

By expressing exponential model of $V(\omega_G)$ in terms of Taylor-series expansion about the operating point $(\overline{\omega}_G, \overline{V})$, the derivative of exponential model can be written by,

$$V\left(\omega_G\right) \approx V\left(\overline{\omega}_G\right) + \left.\frac{dV}{d\omega_G}\right|_{\overline{\omega}_G} \left(\omega_G - \overline{\omega}_G\right) \tag{12}$$

Considering Eq. (12), the slope of exponential model can be linearly approached by three linear equations as follows,

$$V\left(\omega_G\right) = \begin{cases} 5.4146\omega_G - 237.3271, & \overline{\omega}_G = 46 \\ 1.3581\omega_G - 55.4532, & \overline{\omega}_G = 43 \\ 0.3407\omega_G - 12.8871, & \overline{\omega}_G = 40 \end{cases} \tag{13}$$

where these approximations produce error up to 30%. The comparison between linear approximation and exponential model of the voltage is shown in Fig. 5c.

2.4.2 Parameter identification

In order to fit with the Kirchhoff's voltage law, the current equation must be reformed as follows,

$$I\left(\omega_G\right) = k_I\omega_G + I_0 \tag{14}$$

where k_I and I_0 represent current constant (A s/rad) and current's initial condition, respectively. These notations can be obtained from derivative of current from experimental data, which yields in following conditions,

$$\begin{cases} k_I = 0;\ I_0 = 0, & \omega_G < 27.3 \\ k_I = 0.001008;\ I_0 = -0.02573, & \omega_G \geq 27.3 \end{cases} \tag{15}$$

By multiplying constant voltage (k_t) with generator's velocity, the voltage produced by generator with respect to angular velocity can be given as follows,

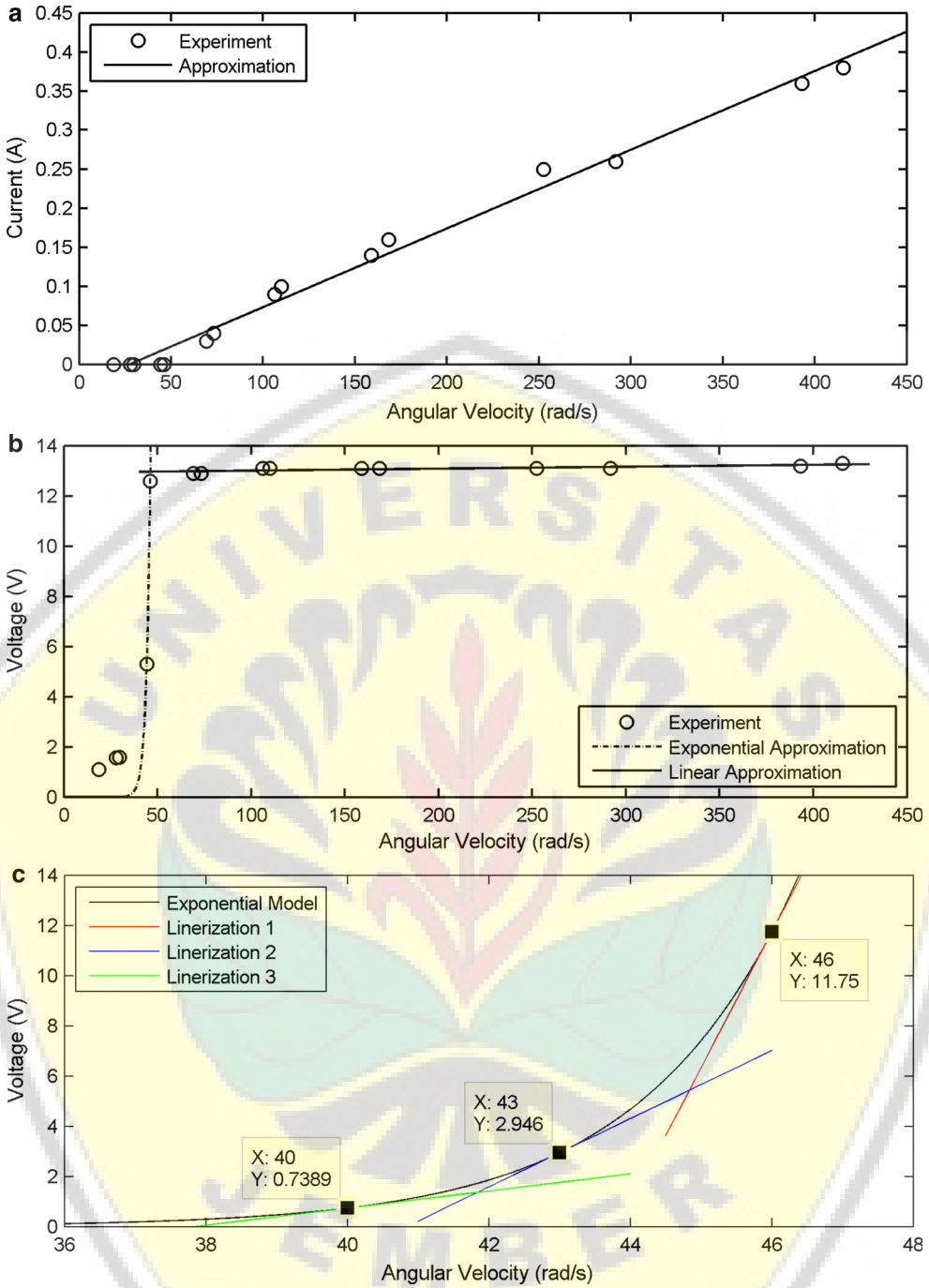

Fig. 5 **a** Plot of electric current with respect to angular velocity; **b** plot of electric voltage and its approximation; **c** linear approximation regarding exponential model of electric voltage

$$V(\omega_G) = k_t \omega_G + V_0 \tag{16}$$

where V_0 designates as voltage's initial condition based on linear approximation from experiment data. Hence, k_t and V_0, obtained from voltage's derivative, can be stated as follows,

$$\begin{cases} k_t = 0;\ V_0 = 0, & \omega_G < 37.83 \\ k_t = 5.415;\ V_0 = -237.327, & 37.83 \le \omega_G < 41.84 \\ k_t = 2.946;\ V_0 = -55.453, & 41.84 \le \omega_G < 44.84 \\ k_t = 2.946;\ V_0 = -55.453, & 44.84 \le \omega_G < 46.23 \\ k_t = 0.000775;\ V_0 = 12.93, & \omega_G \ge 46.23 \end{cases} \tag{17}$$

By associating voltage and current parameters, the electrical torque (T_e) of the generator can be calculated by,

$$T_e = k_e \left(k_I \omega_G + I_0\right) \tag{18}$$

where $k_e = V/\omega_G$.

2.5 Total damping force

The total damping force in this paper is defined as the force required to push the upper plate, so it rotates the bottom plate, epicyclic gears and the generator. Since the velocity in the bottom plate equals with the $Carrier_1$ ($\omega_O = \omega_{c1}$), the full derivation of F can be derived and obtained by combining Eqs. 5, 8 and 9 as follows,

$$F = \frac{J_{CD}\alpha_o + J_{eq}\alpha_{c1} + \left(J_G\alpha_G + T_e\right)\left(\frac{\omega_{s2}}{\omega_{c1}}\right)}{L_{CDZ}\left(\frac{L_{ADZ}}{L_{ADY}}\right) - L_{CDX}\left(\frac{L_{ADX}}{L_{ADY}}\right)} \tag{19}$$

Considering Fig. 1, the velocity of the generator equals with the $Sun\ Gear_2$ ($\omega_G = \omega_{s2}$). The Eq. (19) can be then rewritten by adding T_e from Eq. (18) and the velocity relationship in Eq. (6), which yields,

$$F = \frac{L_{ADY}}{L_{CDZ}L_{ADZ} - L_{CDX}L_{ADX}}\left(J_{CD} + J_{eq} + J_G\left(\frac{\omega_{s2}}{\omega_{c1}}\right)^2\right)\alpha_O + k_e k_I\left(\frac{\omega_{s2}}{\omega_{c1}}\right)^2\omega_O + k_e I_0\left(\frac{\omega_{s2}}{\omega_{c1}}\right) \tag{20}$$

3 Inputs and parameters

In order to take a numerical simulation, inputs and parameters regarding dimensional data of RSA are determined at first. Here we use an input of sinusoidal signal acted in the upper plate which is then be given as follows,

$$\begin{cases} x_A(t) = A\sin\left(2\pi f t\right) \\ \dot{x}_A(t) = 2\pi f A\cos\left(2\pi f t\right) \\ \ddot{x}_A(t) = -\left(2\pi f\right)^2 A\sin\left(2\pi f t\right) \end{cases} \tag{21}$$

where $x_A(t)$, $\dot{x}_A(t)$ and $\ddot{x}_A(t)$ are defined as displacement, velocity and acceleration of the upper plate, respectively. These notations also refer to the velocity and acceleration in A point. In the case $x_A(t) = 0$, the position of the upper plate (L_{ADY}) equals with half of L_{AD}. The motion of $x_A(t)$ can, therefore, be obtained with respect to L_{ADY} by applying,

$$L_{ADY} = x_A(t) + 0.5L_{AD} \tag{22}$$

The mechanical parameters of RSA such as dimensional data in the arm mechanism and epicyclic gears are determined by previous research in [25] and direct measurement, respectively. In the case of moment of inertia, mass and dimension are measured which is then calculated by means of careful drawing in computer aided design software. To sum up, all mechanical parameters including dimension, length, diameter, mass, number of teeth and moment of inertia are listed in Table 1.

4 Results and discussion

Based on the derivative of mathematical models, damping characteristic and energy regeneration are studied under different input of amplitudes and frequencies.

4.1 Damping and energy generated

By setting amplitude and frequency of 0.01 m and 3 Hz, respectively, the time response of damping force generated by the system is shown in Fig. 6a. The red line represents a rebound process while the blue line indicates a compression process. From the response, it is obtained that the rebound process has a sharp form whereas the compression has grad-

Table 1 Mechanical parameters of RSA

Parameter	Value (unit)	Parameter	Value (unit)
$L_{AB} = L_{CD}$	0.05 (m)	J_{c1}	1.0633×10^{-5} (kg m^2)
$L_{AD} = L_{BC}$	0.05 (m)	J_{p1}	6.7584×10^{-8} (kg m^2)
J_{CD}	3.3717×10^{-4} (kg m^2)	J_{c2}	5.7181×10^{-6} (kg m^2)
J_G	1.2778×10^{-7} (kg m^2)	J_{p2}	1.6073×10^{-7} (kg m^2)
n_{p1}	25	$n_1 = n_2$	3
$n_{r1} = n_{r2}$	64	m_{p1}	0.00135 (kg)
n_{s1}	14	m_{p2}	0.00255 (kg)
n_{p2}	28	r_{c1}	0.00975 (m)
n_{s2}	8	r_{c2}	0.011 (m)
$J_{s1} = J_{s2}$	1.2778×10^{-7} (kg m^2)		

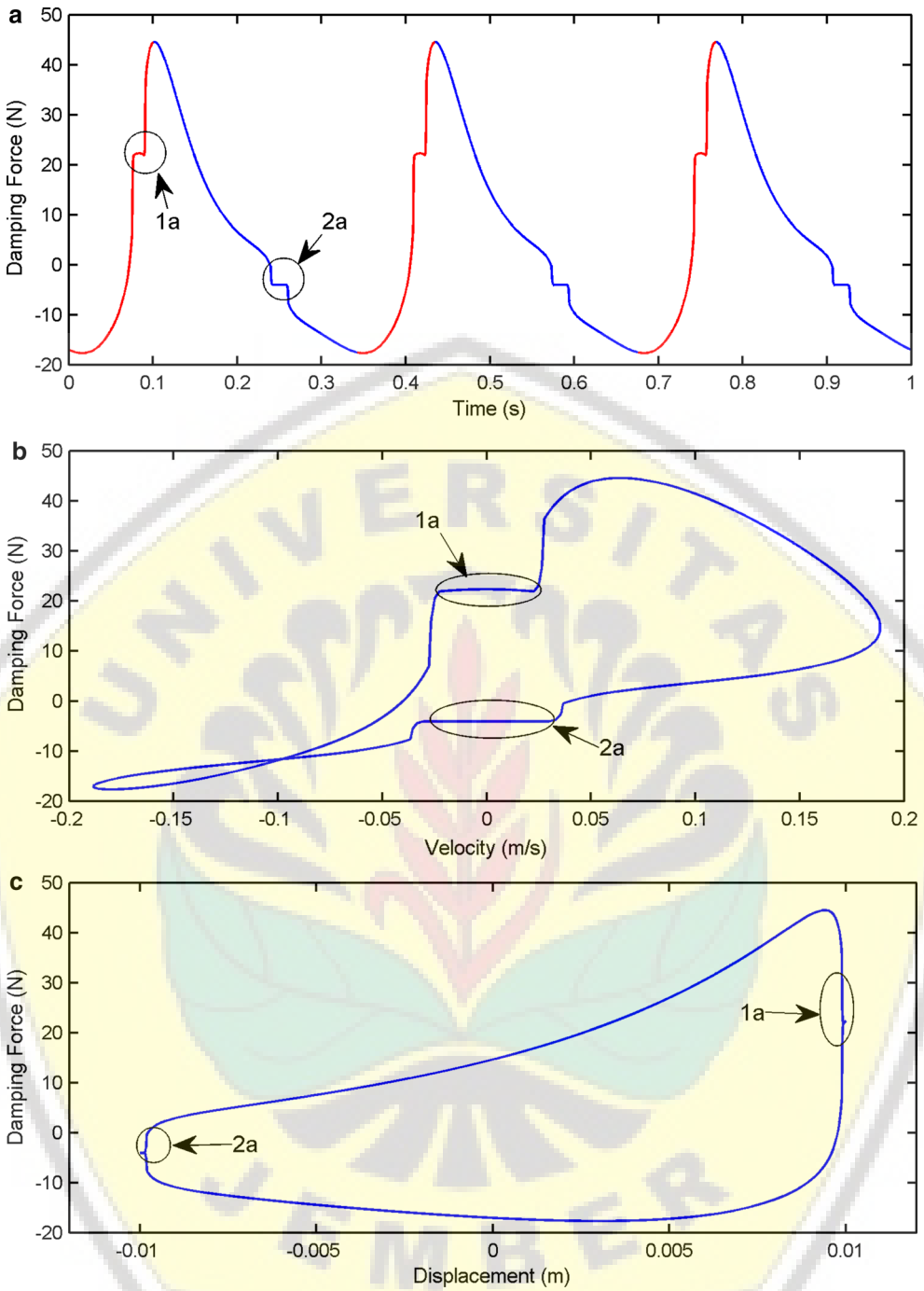

Fig. 6 Total damping force in **a** time response; **b** velocity response; and **c** displacement response

ually changes. The peak and valley are found at 44.55 and 17.69 N, respectively. These differences can be investigated from the position of the upper plate and bottom plate. When the damping force reaches at the maximum value (positive sign), the upper plate is in the farthest point from the bottom plate. At this condition, the angle of the bottom plate is particularly small regarding Fig. 3 so the highest force will be achieved in this stage. On the other hand, the smaller damping force is produced when the angle is determined at the highest value or the position of the upper plate and bottom plate at the closest point.

The total damping force is then plotted with respect to velocity as shown in Fig. 6b. It can be seen that the lags in time response, mentioned with circle 1a and 2a, are occurred when changing velocity from positive to negative or vice versa. Meanwhile, the curve is overlapped each other in the

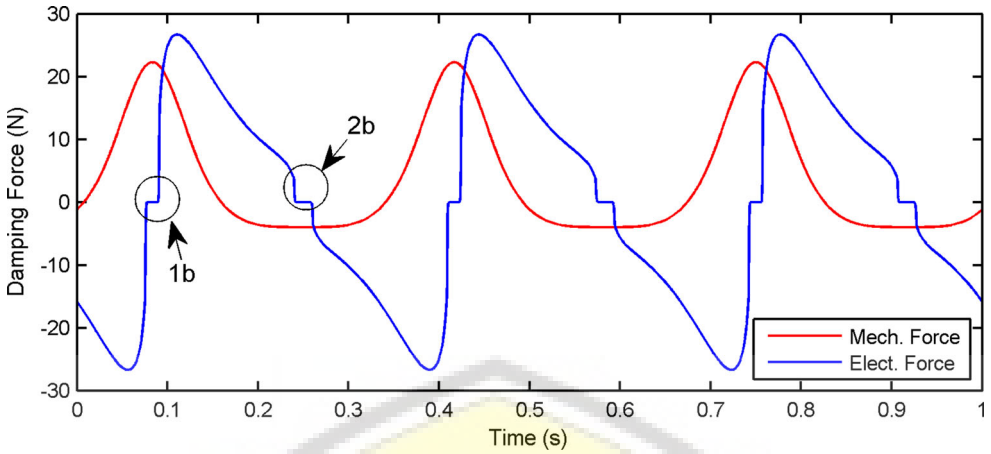

Fig. 7 Damping generated by mechanical and electrical force in time series

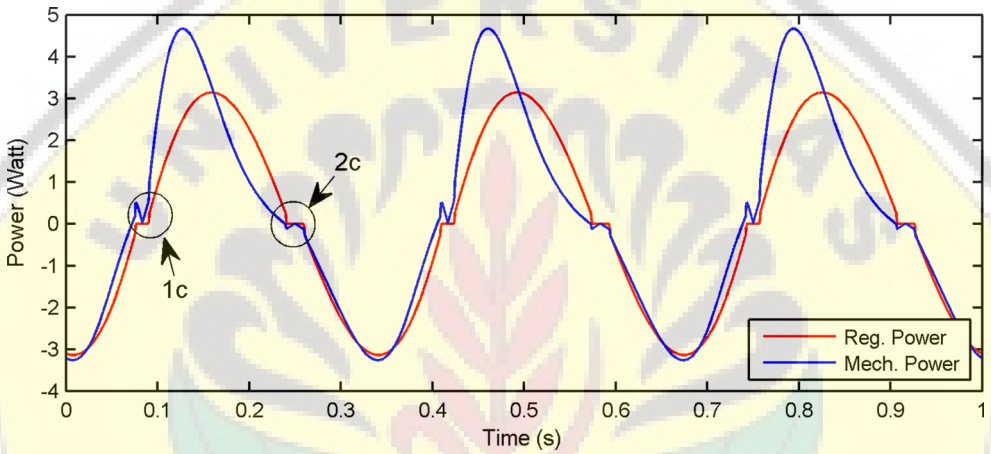

Fig. 8 Power generated by the RSA in time series

velocities of -0.1 to -0.19 m/s. This can refer to the time series plot in Fig. 6a, where the rebound stage has less time compared with the compression stage near the valley. In addition, the force is also depicted in term of displacement as shown in Fig. 6c. As integral of velocity, the circle number of 1a and 2a are located at near the maximum and minimum of displacement. This reveals that those phenomena can be caused by the parameter, which has the velocity function.

To give a better understanding, the mechanical and electrical forces, which is the main components in forming the total damping force, are explored in time series as depicted in Fig. 7a. From the figure, the red line represents the mechanical force composed by mass moment of inertia of the bottom plate, epicyclic gears and generator, while the blue line signifies the electrical force derived from electrical torque in Eq. (18) of the generator. Hence, the lag of circle 1a Fig. 6a is caused by a dead zone in the electrical force whilst the mechanical force reaches peak as shown in Fig. 7a. The same pattern also occurs in circle number 2a, where the electrical force is in the compression mode from positive to negative sign. In addition, the dead zones in electrical force, marked with circle 1b and 2b in Fig. 7a, can be linked with current generated with respect to angular velocity in Eq. (10). In that case, the angular velocity is under 27.31 rad/s that means the current will be at zero value as plotted in Fig. 5a.

Figure 8 shows the comparison between the mechanical and regenerative power in time history as indicated with blue line and red line, respectively. The maximum value for the mechanical and regenerative power is achieved at 4.67 and 3.14 W, respectively. This means that the efficiency of the RSA lies on 67.29%. In other words, the RSA can covert 67.29% of mechanical energy into electrical energy, while 32.71% is dissipated in other forms such as frictional losses and inertial losses occurred in the arm mechanism, generator and combined epicyclic gears. In the case of the power in negative value, the gap between the mechanical and regenerative power is small, where it is resulted from the small generation of the mechanical force in negative sign as described in Fig. 7. This occasion can be cross-linked with the delays in the peak and valley. The peak has a larger lag that can be caused by

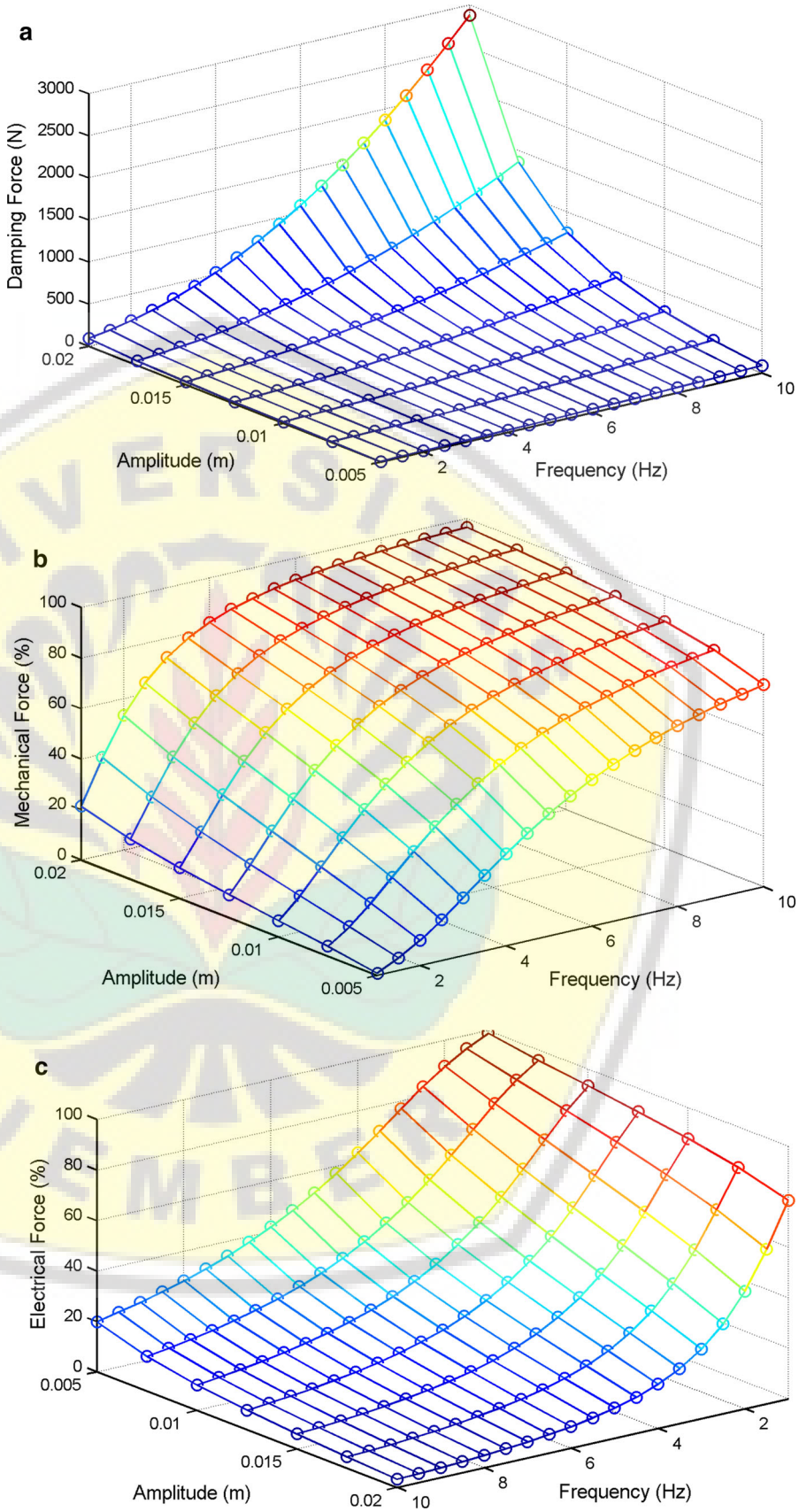

Fig. 9 **a** Total damping force; percent contribution of **b** the mechanical force and **c** the electrical force

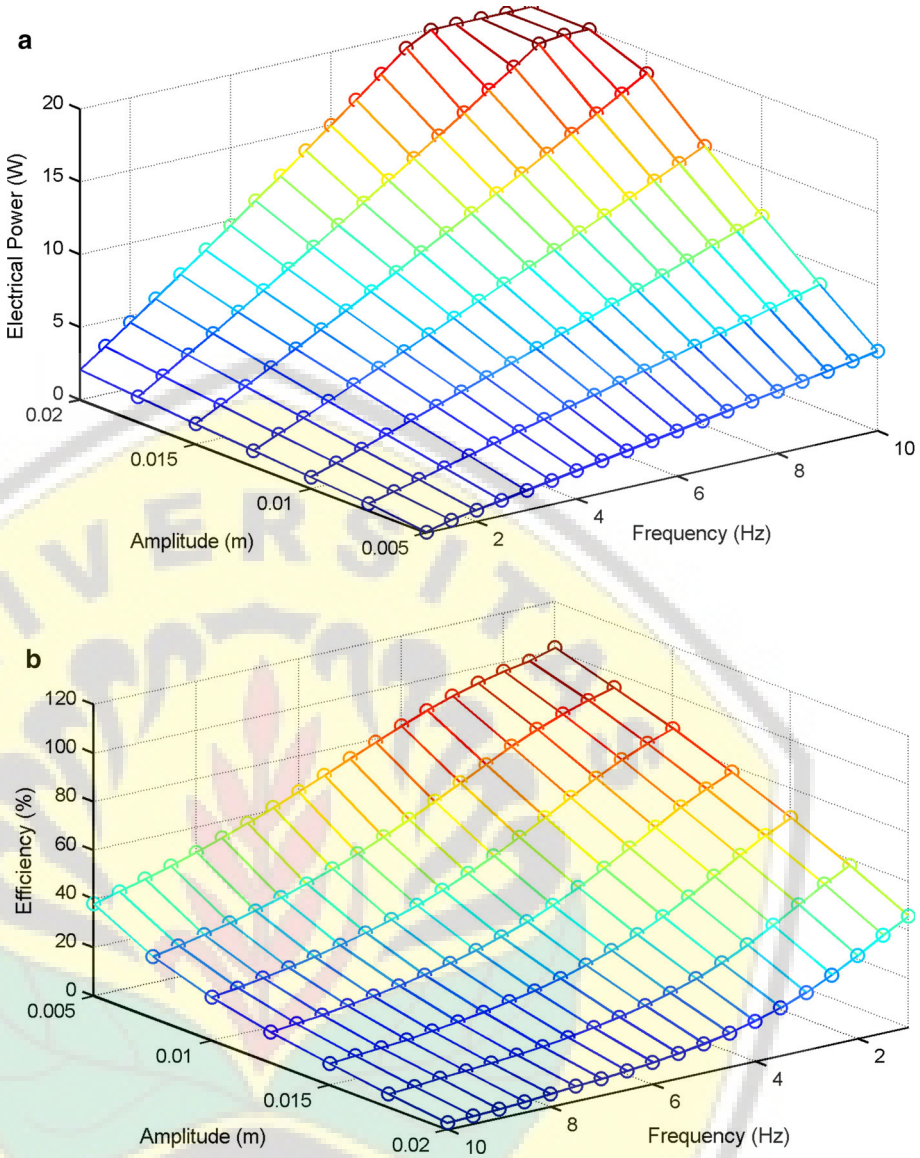

Fig. 10 **a** Power generated by system; **b** efficiency of the RSA regarding amplitudes and frequencies

the influences of velocity function and acceleration function, whereas the valley has nearly similar that resulted from the electrical force derived from fully velocity function. Furthermore, the dent as circled with number 1c and 2c is induced from the same causes as aforementioned in Figs. 6 and 7.

4.2 Influence of amplitude and frequency

Figure 9a shows the maximum value of the total damping force in difference amplitudes and frequencies. Overall, the damping force is raised up as increasing amplitude and frequency. As aforementioned, for example in Fig. 6a, the peak of 44.5 N at time of 0.1017 s encompasses of 19.04 and 25.51 N of the mechanical and electrical force, respectively. It means that the mechanical force contributes of 42.74% while the electrical force gives percentage of 57.26%. Thus, the contribution percentages are plotted with regard to amplitudes and frequencies as shown in Fig. 9b, c for representing mechanical and electrical force, respectively.

In Fig. 9b, c, it can be inferred that the damping force is dominated by the mechanical force in high amplitude and frequency range. Meanwhile, the percentage of the electrical force is worth for frequency up to 2 Hz, which gives the proportion more than two fifths for all amplitudes. Increasing the mechanical force proportion will decrease the efficiency of the energy regeneration. Otherwise, increasing the electrical force will be directly proportional to the regeneration efficiency. It is because the electrical force, formed by the electric torque, only contains of volt and current parameters, which are the main components determining the regeneration power as described in Eq. (18).

Figure 10a describes the power generated by the energy regeneration unit. It can be supposed that increasing amplitude and frequency will increase the output of the power generation. Nevertheless, the power will be no longer increased and come to steady after the maximum power generation of the generator is reached at 20 W. The efficiency of energy regeneration is plotted in 3D surface as shown in Fig. 10. The behavior is close to the percentage of the electrical force and counteracts with the regeneration power. The best working range of amplitude and frequency is bounded by the yellow color that gives a percentage more than half. In the starting amplitude and frequency range (0.005 m and 1 Hz), the efficiency reaches 101.3%. This abnormality is caused by the linear approximation of Eq. (10) depicted in Fig. 5a. From the experimental data, the current will be zero until the angular velocity is greater than or equal to 46.15 rad/s. In a different way, the linear approximation creates zero intersection in the angular velocity of 27.31 rad/s. It means that the zero is displaced along 18.84 rad/s from the origin, which creates the efficiency for slightly more than 100%.

5 Conclusion

In this research, the force characteristic and energy regeneration have been presented. The mathematical models and parameters were derived and studied. The damping force shows promising asymmetry where it is fully influenced by the arm mechanism and mechanical parameters. On the other hand, electrical parameters have contribution in symmetrical form in both rebound and compression mode. It is possible to reduce the percentage of mechanical force that will be resulted in increasing the regeneration efficiency. However, the damping pattern will be highly affected by electrical force, which reduces asymmetrical characteristics of the RSA. Another advantage from this RSA is in the energy regeneration side, which has the same characteristics both in rebound and compression mode regardless of bidirectional motion occurred in the generator. Overall, it is clear to see the differences of this RSA compared with the other RSA that has asymmetrical properties in the damping generated and symmetrical properties in the energy regeneration. In the further study, it is essential to develop experimental test in order to conduct validation with derived mathematical models. The RSA also needs to investigate in a simplified vehicle model to gain the transmissibility, stability and ride comfort comparing with TSA.

Acknowledgements This work is funded by the Directorate for Research and Community Service – Directorate General of Research and Development Strengthening – Ministry of Research, Technology and Higher Education of the Republic of Indonesia based on the decision number 025/E3/2017.

Appendix

In order to obtain the position, velocity and acceleration of the arm mechanism, we take the advantage of symmetrical structure in the arm mechanism. Here the kinematics analysis is performed one side only by considering the rod AD as the main interest for determining θ_O, ω_O and α_O which yields,

$$\theta_O = \cos^{-1}\left(\frac{L_{ADY}^2 + 0.025\left(L_{CD}^2 + L_{AB}^2\right) - L_{AD}^2}{0.05 L_{CD} L_{AB}}\right),$$

$$\omega_O = -\left(\frac{L_{ADZ}L_{ADY} + \left(L_{ADY}^2 + L_{ADX}^2\right)\varphi}{L_{ADX}\left(L_{ADZ}^2 + L_{ADX}^2 + L_{ADZ}L_{ADY}\varphi\right)}\right)\dot{x}_A,$$

$$\begin{aligned}\alpha_O = {} & \frac{1}{L_{ADX}}\left(\left(\omega_{ADY}^2 - \omega_{ADX}^2\right)L_{ADZ} + \omega_{ADZ}\omega_{ADX}L_{ADX}\right. \\ & \left. - \omega_{ADY}\omega_{ADZ}L_{ADY} + 0.5\omega_O^2 L_{CD}\cos\theta_O + \frac{L_{ADY}^2 + L_{ADX}^2}{L_{ADX}}\psi\right) \\ & - \frac{L_{ADZ}L_{ADY} + \left(L_{ADY}^2 + L_{ADX}^2\right)\varphi}{L_{ADX}\left(L_{ADZ}^2 + L_{ADX}^2 + L_{ADZ}L_{ADY}\varphi\right)} \\ & \left(\left(\omega_{ADX}^2 + \omega_{ADZ}^2\right)L_{ADY}\right. \\ & + \omega_{ADZ}\omega_{ADY}L_{ADZ} \\ & \left. - \omega_{ADY}\omega_{ADX}L_{ADX} + \ddot{x}_A + \frac{L_{ADZ}L_{ADY}}{L_{ADX}}\psi\right),\end{aligned}$$

where

$$\begin{aligned}L_{ADX} &= 0.5 L_{CD}\sin\theta_O, \\ L_{ADZ} &= 0.5\left(L_{AB} - L_{CD}\cos\theta_O\right), \\ \varphi &= \frac{L_{ADY}L_{ADX}\tan\theta_O + L_{ADY}L_{ADX}}{L_{ADY}L_{ADX}\tan\theta_O - L_{ADY}^2 - L_{ADX}^2}, \\ \omega_{ADX} &= \frac{\dot{x}_A}{L_{ADZ}}\left(\frac{L_{ADX}^2}{L_{ADZ}^2 + L_{ADX}^2 + L_{ADZ}L_{ADY}\varphi} - 1\right), \\ \omega_{ADZ} &= \frac{\dot{x}_A L_{ADX}}{L_{ADZ}^2 + L_{ADX}^2 + L_{ADZ}L_{ADY}\varphi}, \\ \omega_{ADY} &= \omega_{ADZ}\varphi,\end{aligned}$$

References

1. Lafarge, B., Cagin, S., Curea, O., Perret, A.H.: From functional analysis to energy harvesting system design: application to car suspension. Int. J. Interact. Des. Manuf. IJIDeM **10**(1), 37–50 (2015). https://doi.org/10.1007/s12008-015-0284-1
2. Maravandi, A.: Design and implementation of a regenerative shock absorber. PhD Thesis, Simon Fraser University (2015)
3. Hendrowati, W., Guntur, H.L., Sutantra, I.N.: Design, modeling and analysis of implementing a multilayer piezoelectric vibration energy harvesting mechanism in the vehicle suspension. Engineering **04**(11), 728–738 (2012). https://doi.org/10.4236/eng.2012.411094

4. Zhang, P.S.: Design of electromagnetic shock absorbers for energy harvesting for energy harvesting from vehicle suspensions. Master Thesis, Stony Brook University (2010)
5. Konieczny, Ł.: Analysis of simplifications applied in vibration damping modelling for a passive car shock absorber. Shock Vib. **2016**, 1–9 (2016). https://doi.org/10.1155/2016/6182847
6. Silveira, M., Pontes, B.R., Balthazar, J.M.: Reducing vertical and angular accelerations with nonlinear asymmetrical shock absorber in passenger vehicles, p. V008T013A026 (2013). https://doi.org/10.1115/detc2013-12241
7. Silveira, M., Pontes, B.R., Balthazar, J.M.: Use of nonlinear asymmetrical shock absorber to improve comfort on passenger vehicles. J. Sound Vib. **333**(7), 2114–2129 (2014). https://doi.org/10.1016/j.jsv.2013.12.001
8. Li, Z., Zuo, L., Luhrs, G., Lin, L., Qin, Y.-X.: Electromagnetic energy-harvesting shock absorbers: design, modeling, and road tests. IEEE Trans. Veh. Technol. **62**(3), 1065–1074 (2013). https://doi.org/10.1109/tvt.2012.2229308
9. Zhang, Z., Zhang, X., Chen, W., Rasim, Y., Salman, W., Pan, H., Yuan, Y., Wang, C.: A high-efficiency energy regenerative shock absorber using supercapacitors for renewable energy applications in range extended electric vehicle. Appl. Energy **178**, 177–188 (2016). https://doi.org/10.1016/j.apenergy.2016.06.054
10. Tonoli, A., Amati, N., Detoni, J.G., Galluzzi, R., Gasparin, E.: Modelling and validation of electromechanical shock absorbers. Veh. Syst. Dyn. **51**(8), 1186–1199 (2013). https://doi.org/10.1080/00423114.2013.789538
11. Maravandi, A., Moallem, M.: Modeling and design of a motion converter for utilization as a vibration energy harvester, pp. 4204–4209 (2013). https://doi.org/10.1109/iecon.2013.6699810
12. Sabzehgar, R., Maravandi, A., Moallem, M.: Energy regenerative suspension using an algebraic screw linkage mechanism. IEEE/ASME Trans. Mechatron. **19**(4), 1251–1259 (2014). https://doi.org/10.1109/tmech.2013.2277854
13. Ebrahimi, B., Khamesee, M.B., Golnaraghi, M.F.: Design and modeling of a magnetic shock absorber based on eddy current damping effect. J. Sound Vib. **315**(4–5), 875–889 (2008). https://doi.org/10.1016/j.jsv.2008.02.022
14. Zuo, L., Scully, B., Shestani, J., Zhou, Y.: Design and characterization of an electromagnetic energy harvester for vehicle suspensions. Smart Mater. Struct. **19**(4), 045003 (2010). https://doi.org/10.1088/0964-1726/19/4/045003
15. Fang, Z., Guo, X., Xu, L., Zhang, H.: Experimental study of damping and energy regeneration characteristics of a hydraulic electromagnetic shock absorber. Adv. Mech. Eng. **5**, 943528 (2013). https://doi.org/10.1155/2013/943528
16. Guo, S., Xu, L., Liu, Y., Liu, M., Guo, X., Zuo, L.: Modeling, experiments, and parameter sensitivity analysis of hydraulic electromagnetic shock absorber. V003T001A032 (2016). https://doi.org/10.1115/detc2016-60390
17. Li, C., Zhu, R., Liang, M., Yang, S.: Integration of shock absorption and energy harvesting using a hydraulic rectifier. J. Sound Vib. **333**(17), 3904–3916 (2014). https://doi.org/10.1016/j.jsv.2014.04.020
18. Zhang, H., Guo, X., Xu, L., Hu, S., Fang, Z.: Parameters analysis of hydraulic-electrical energy regenerative absorber on suspension performance. Adv. Mech. Eng. **6**, 836502 (2015). https://doi.org/10.1155/2014/836502
19. Zhang, Y., Zhang, X., Zhan, M., Guo, K., Zhao, F., Liu, Z.: Study on a novel hydraulic pumping regenerative suspension for vehicles. J. Frankl. Inst. **352**(2), 485–499 (2015). https://doi.org/10.1016/j.jfranklin.2014.06.005
20. Guntur, H.L., Hendrowati, W., Lubis, R.R.: Development and analysis of a regenerative shock absorber for vehicle suspension. J. Syst. Des. Dyn. **7**(3), 304–315 (2013). https://doi.org/10.1299/jsdd.7.304
21. Li, Z., Zuo, L., Kuang, J., Luhrs, G.: Energy-harvesting shock absorber with a mechanical motion rectifier. Smart Mater. Struct. **22**(2), 025008 (2013). https://doi.org/10.1088/0964-1726/22/2/025008
22. Syuhri, S.N.H., Ilminnafik, N.: Damping force and energy regeneration characteristics of the regenerative pendulum vibration absorber. Appl. Mech. Mater. **865**, 434–441 (2017). https://doi.org/10.4028/www.scientific.net/AMM.865.434
23. Maravandi, A., Moallem, M.: Regenerative shock absorber using a two-leg motion conversion mechanism. IEEE/ASME Trans. Mechatron. **20**(6), 2853–2861 (2015). https://doi.org/10.1109/tmech.2015.2395437
24. Roshan, Y.M., Maravandi, A., Moallem, M.: Power electronics control of an energy regenerative mechatronic damper. IEEE Trans. Ind. Electron. **62**(5), 3052–3060 (2015). https://doi.org/10.1109/tie.2015.2392714
25. Syuhri, A., Basuki, H.A., Syuhri, S.N.H.: Kinematics analysis of a leg mechanism as a motion converter. Int. Rev. Mech. Eng. IREME **10**(6), 409 (2016). https://doi.org/10.15866/ireme.v10i6.10011